Optimized Demagnetizing Control of DFIG Power Converter for Reduced Thermal Stress During Symmetrical Grid Fault

Dao Zhou, *Member, IEEE* and Frede Blaabjerg, *Fellow, IEEE*

***Abstract*—Direct linking between the stator of a doubly fed induction generator (DFIG) and the power grid makes this type of generator sensitive to disturbances in the grid voltage, which may lead to high voltage and current on the rotor side. Moreover, modern grid codes, which specify stringent requirements on reactive power compensation, challenge fault ride-through operation even more. In this paper, based on conventional demagnetizing current control, the capability of a DFIG rotor-side converter to ride-through a symmetrical grid fault is calculated in accordance with its current and voltage ratings. Afterwards, an optimized demagnetizing coefficient is designed to guarantee the same rotor current amplitude between the instants of the fault occurrence and the reactive current injection. A reduction of the junction temperature of the power device can thereby be achieved. It is concluded that, regardless of the rotor speed, the demagnetizing coefficient is related only to the dip level. Compared with traditional vector control, a simulation of 2 MW DFIG system agrees with the reduced thermal stress during the fault period, and experimental results in a down-scale DFIG system verify the feasibility of the proposed control strategy as seen from the electrical characteristics.**

***Index Terms*—Current control, doubly fed induction generator (DFIG), low-voltage ride-through, thermal stress.**

I. Introduction

A RECENT study by the Danish Energy Agency indicates that onshore wind power is the cheapest form of renewable electricity generation in Denmark [1]. Owing to the noise emission and footprint limitation, it is more promising to move wind turbines offshore, where their lifespan is prolonged and expected to be 20–25 years [2], [3]. As one of the most vulnerable components in a turbine system, increasing number of research efforts have been devoted to the reliable operation of the power electronic converter because of its time-consuming and expensive maintenance [4], [5]. However, faulty situations in the power grid caused by lightning, hurricanes, or equipment tripping may induce over-current and over-voltage issues in the power converter. Thus, a robust solution is preferred and encouraged for the long-term cost-effective operation of wind turbines.

The doubly fed induction generator (DFIG) is a widely used configuration for wind turbines with power generation capacity higher than 1 MW, as it provides the advantage of variable speed operation and full control of active and reactive power using a converter with only a small fraction of the rated power (20%–30%) [6]. However, upon detecting a grid fault, the generator unit is usually disconnected to protect the vulnerable rotor-side converter (RSC), by using the rotor-side crowbar [7]–[9]. This approach makes the DFIG a traditional squirrel-cage motor, absorbing reactive power from the grid, which is against modern grid codes [10], [11]. Another hardware solution for fault ride-through is to apply a dynamic voltage restorer or a series grid-side converter (GSC) between the stator and the grid, as they facilitate a smooth stator voltage and eliminate the transient stator flux [12]–[14]. These hardware solutions address the disadvantages such as additional ancillary control and increased cost.

With the merits of easy adoption and cost-effectiveness, many researchers turn to software solutions when facing grid faults [15]–[19]. It has been demonstrated that the rotor current is limited by using a feed-forward transient current control [16], and the stator current is directly fed back as a rotor current reference to suppress the fault current [17]. In addition, the demagnetizing control is a popular solution for eliminating the natural stator flux [18], [19]. Owing to the assumption that the natural stator flux should be removed as soon as possible, the demagnetizing coefficient is designed at the maximum rating of the rotor current [18]. However, this is not fully appropriate when the transient thermal performance of the power semiconductor is considered. As a lot of work has been carried out to evaluate the reliability of power converters used in wind power applications [20]–[22], it is generally accepted that the thermal profile of a power semiconductor is an important indicator of the reliability assessment. Based on the DFIG steady-state and the transient models during the fault period, this paper aims to calculate the fault ride-through capability of the power converter through its rating. Then, an optimized demagnetizing control can be selected from this range, and designed from the minimum junction temperature of the power semiconductor during a fault period, which is closely related to the parameters of the DFIG and its RSC, the grid fault severity and the grid codes requirement.

Manuscript received March 28, 2017; revised September 8, 2017 and December 11, 2017; accepted January 22, 2018. Date of publication February 7, 2018; date of current version September 28, 2018. Recommended for publication by Associate Editor M. T. Bina. *(Corresponding author: Dao Zhou.)*

D. Zhou is with the Department of Energy Technology, Aalborg University, Aalborg, DK- 9220, Denmark (e-mail: zda@et.aau.dk).

F. Blaabjerg is with the Department of Energy Technology, Aalborg University, Aalborg, DK- 9220, Denmark (e-mail: fbl@et.aau.dk).

Color versions of one or more of the figures in this paper are available online at http://ieeexplore.ieee.org.

Digital Object Identifier 10.1109/TPEL.2018.2803125

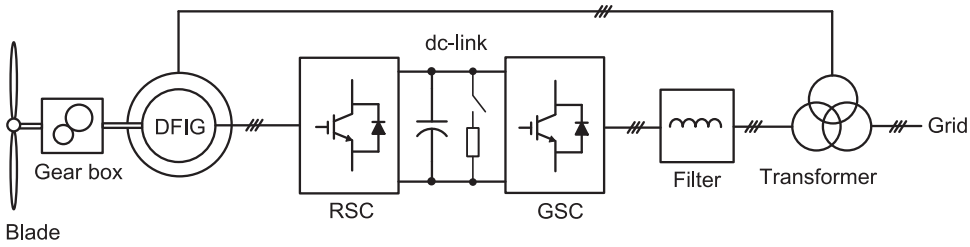

Fig. 1. Typical configuration of the doubly fed induction generator (DFIG) wind turbine system. (GSC: Grid-side converter. RSC: Rotor-side converter).

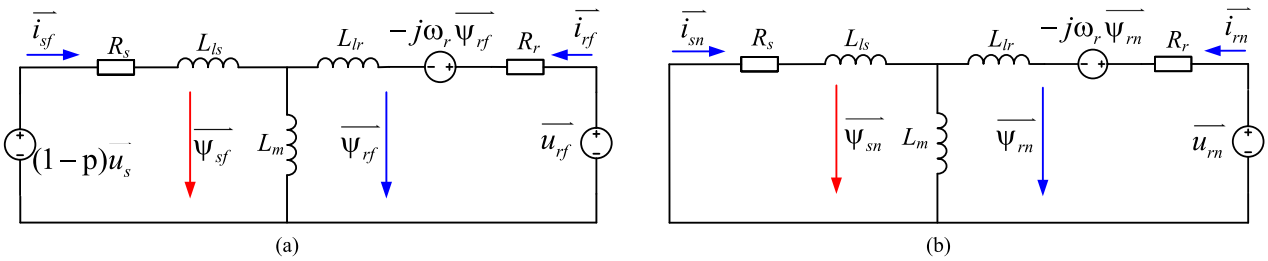

Fig. 2. Dynamic model of the DFIG under a symmetrical grid fault. (a) Forced machine. (b) Natural machine.

The structure of this paper is as follows. Section II addresses the modeling and challenges of a DFIG when facing a symmetrical grid fault. In Section III, the relationship between the rotor voltage and rotor current is investigated by using demagnetizing control, and the capability of the DFIG is thereby calculated. Afterwards, the effects of the reactive current injection and the effects of the residual demagnetizing current are theoretically analyzed, and a design procedure for an optimized demagnetizing coefficient is introduced, which facilitates minimum thermal stress of the RSC. Based on simulations in a real-scale wind turbine and experiments in a down-scale setup in Section V, concluding remarks are drawn in the last section.

II. Existing Issues of DFIG Facing Symmetrical Grid Fault

This section begins with a description of the DFIG model in terms of voltage equations and flux equations under a symmetrical grid fault. The internal challenge for the fault ride-through lies in the introduction of the natural stator flux, caused by the direct connection between the DFIG stator and the power grid, while the external challenge comes from the reactive current injection imposed by the grid codes.

A. Internal Challenge from DFIG Configuration

A typical DFIG configuration is depicted in Fig. 1, where the RSC and the GSC are named owing to their positions. By using the stator reference frame, the voltage and flux equations of the stator side and rotor side are

$$\vec{u}_s^s = R_s \vec{i}_s^s + \frac{d}{dt}\vec{\psi}_s^s \tag{1}$$

$$\vec{u}_r^s = R_r \vec{i}_r^s + \frac{d}{dt}\vec{\psi}_r^s - j\omega_r \vec{\psi}_r^s \tag{2}$$

$$\vec{\psi}_s^s = L_s \vec{i}_s^s + L_m \vec{i}_r^s \tag{3}$$

$$\vec{\psi}_r^s = L_m \vec{i}_s^s + L_r \vec{i}_r^s \tag{4}$$

where u, i, and ψ denote the voltage, current and flux, respectively. R and L denote the resistance and inductance, the subscripts s and r denote the stator quantities and rotor quantities, the superscript s denotes the stator reference frame, L_m denotes the mutual inductance, and ω_r denotes the rotor angular frequency.

The natural stator flux is inevitably introduced in the case of a symmetrical grid fault, while both the natural and negative stator flux may be produced in the case of an asymmetrical fault [23]. Although the stator flux may contain a component that is separate from the grid frequency, (1)–(4) remain effective and can be used as the dynamic model of the DFIG. As the stator of the DFIG is directly linked to the power grid, the stator flux cannot be changed abruptly during the occurrence of a grid disturbance. In the case of a symmetrical grid fault with a dip level p, the components of the stator flux can be divided into the forced stator flux and the natural stator flux [19]. The forced stator flux is caused by the remaining grid voltage, while the natural stator flux is introduced owing to the continuity of the flux evolution. Consequently, the dynamic model of the DFIG can be divided into a forced machine and a natural machine, as shown in Fig. 2, where subscripts f and n represent quantities under the forced machine and the natural machine, respectively.

Neglecting the insignificant voltage drop of the stator resistance, and assuming the implementation of a vector control (i.e., no natural component of the rotor current is expected), the stator flux consists of the forced component and natural component according to (1)

$$\vec{\psi}_s^s(t) \approx \frac{(1-p)U_s}{j\omega_1} e^{j\omega_1 t} + \frac{pU_s}{j\omega_1} e^{-\frac{t}{\tau_s}} \tag{5}$$

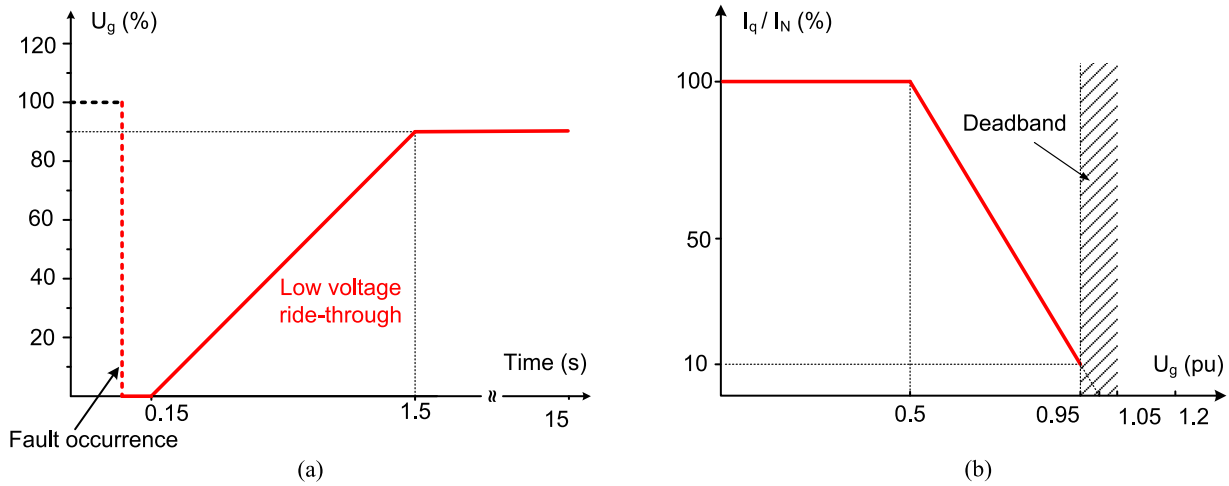

Fig. 3. Wind turbine requirements under grid disturbance [10]. (a) Voltage ride-through. (b) Reactive current injection during ride-through.

where U_s denotes the amplitude of the normal grid voltage, ω_1 denotes the grid angular frequency, and τ_s denotes the time constant of the stator flux, which equals L_s/R_s. In multimegawatt DFIGs, this time constant ranges between hundreds of milliseconds and several seconds, which are normally much longer than the fault duration. In addition, the forced flux rotates with a synchronous speed with respect to the stator winding, while the newly introduced natural flux stands still with respect to the stator winding.

According to (2)–(4), the rotor voltage can be represented by the rotor current and the stator flux

$$\vec{u}_r^r = R_r \vec{i}_r^r + \sigma L_r \frac{d}{dt}\vec{i}_r^r + \frac{L_m}{L_s}\frac{d}{dt}\vec{\psi}_s^r \tag{6}$$

where σ denotes the leakage inductor coefficient $\sigma = 1 - L_m^2/L_s L_r$, and superscript r denotes the rotor reference frame. The first and second items represent the voltage drop across the rotor resistance and rotor inductor caused by the rotor current, and the third item represents the electromotive force (EMF) e_r, which is almost the differential of the stator flux.

Substituting (5) into (6), owing to the small stator leakage inductance compared to the mutual inductance of the induction machine, together with the insignificance of the stator flux decaying frequency compared to the rotor angular frequency, the EMF is approximately

$$\vec{e}_r^r(t) \approx s(1-p)U_s e^{j(\omega_1-\omega_r)t} - (1-s)pU_s e^{-j\omega_r t}. \tag{7}$$

Since the slip value of the DFIG, s normally varies from -0.25 to 0.25, it can be inferred that the natural component of the EMF may be much higher than the forced component of the EMF in the case of high dip levels (e.g., higher than 0.5). In the normal grid condition, the dc-link voltage is designed and regulated based on the forced machine of the DFIG. As a result, a symmetrical grid fault may lead to the saturation of the RSC, and potential over-voltage and over-current issues may prevent the DFIG ride-through operation.

B. External Challenge from Grid Codes

Although a severe grid fault may cause saturation of the RSC and loss of the control of the rotor current, modern grid codes rarely encourage disconnection of the DFIG to be from the grid, owing to the high penetration of renewable energy. German grid codes are shown in Fig. 3(a), and it is noted that a wind turbine system is generally required to remain connected for a certain period with various dip levels, even at 150 ms for the zero voltage.

Apart from the fault ride-through of the DFIG itself, the reactive current is provided to the power grid within dozens or hundreds of milliseconds after the voltage dip. As shown in Fig. 3(b), the higher dip level demands a larger reactive current, and up to 1.0 pu reactive current is expected if the dip level is higher than 0.5. The requirement of the reactive current injection results in an additional increase of the rotor current and can be considered an external challenge of the fault ride-through.

III. DFIG Capability and Performance by Using Demagnetizing Control

This section begins with an introduction to demagnetizing control. Subsequently, the capability and performance of the DFIG under a grid fault can be investigated and calculated by using the demagnetizing control.

A. Demagnetizing Control

As expressed in (7), since the forced component of the rotor EMF is linearly related to the slip s, while the natural component of the rotor EMF is proportional to $(1-s)$, it can be expected that the natural machine mainly determines the saturation of the RSC. However, traditional vector control only takes care of the forced machine and provides the rotor current at the slip angular frequency, which hardly contributes to canceling out the natural component of the rotor EMF.

According to (6), the relationship between the rotor voltage and the rotor current is shown in Fig. 4(a) under the natural machine. As shown in Fig. 4(b), it is noted that the natural stator flux lags the stator voltage by 90°, and the rotor EMF again

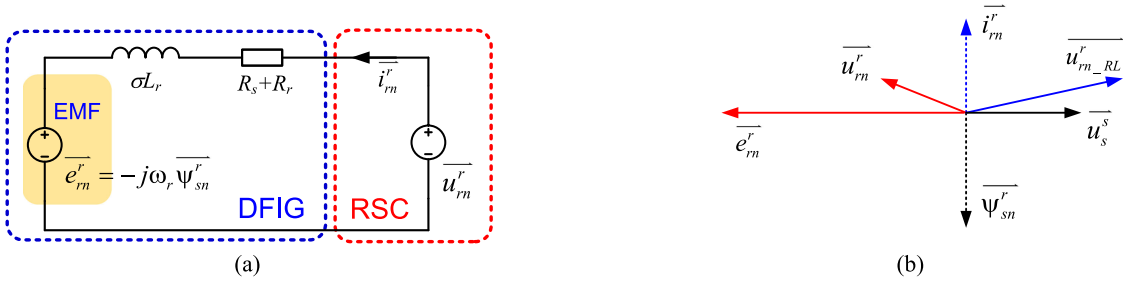

Fig. 4. Relationship between the rotor voltage and the rotor current under the natural machine. (a) Equivalent DFIG model seen from the rotor. (b) Phasor diagram of the DFIG under the rotor reference frame.

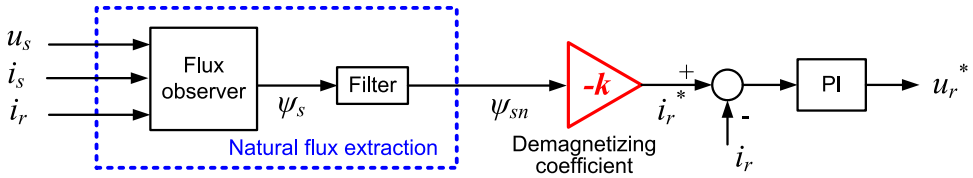

Fig. 5. Control diagram for the demagnetizing control strategy.

lags the natural flux by 90°. In addition, owing to the inductive characteristic of the DFIG rotor side, the voltage drop across the rotor side $u_{\mathrm{rn\_RL}}$ lags the rotor current by almost 90°.

Demagnetizing control is used to reduce the rotor voltage during a grid fault. It tries to regulate the rotor current in the opposite direction of the natural stator flux, as shown in Fig. 5 [18], [19]. Compared with traditional vector control, a flux observer is introduced to obtain the stator flux, which is estimated through the stator voltage, stator current, and rotor current [24]. Compared to the open-loop scheme mentioned in [18], a PI correction loop is employed to compensate the dc-bias introduced by the integrator. Further, this flux observer shows a small sensitivity to the stator resistance and the magnetizing inductance detuning. Then, the natural stator flux can be extracted from the stator flux with the help of a notch filter. The stator flux under a stator reference frame is changed into a synchronous reference frame. Thus, the forced and natural stator flux becomes a dc component and an ac component with 50 Hz, respectively. A second-order notch filter with a damping factor of 0.22 and frequency of 50 Hz can be applied to well separate the natural and forced stator flux. However, by using a stator flux observer and a notch filter, the estimated flux may contain phase and magnitude errors; these effects are not taken into account in this paper. By the definition of the demagnetizing coefficient k, the modulated rotor voltage u_r^* can be obtained by using a PI controller. Because the preferred current contributes solely to absorbing the reactive power, the demagnetizing control is regarded as the most effective way to overcome the transient natural flux. However, an extra control freedom exists: the demagnetizing coefficient.

B. Capability of DFIG

With the specifications of the induction generator as well as the important parameters of the RSC listed in Tables I and II, a case study is performed on a 2 MW DFIG system. The safety operation area (SOA) of the RSC is closely related to the capacity of the power semiconductors. Together with the power semiconductor ratings and the rated rotor current listed in Table II, it is evident that the RSC can support up to a 2.0 pu rotor current. Moreover, a 1050 V dc-link voltage at a full modulation index can be transferred into a 2.0 pu rotor voltage. For a

TABLE I
SPECIFICATION OF DOUBLY FED INDUCTION GENERATORS

Rated power	2 MW	7.5 kW
Operational range of rotor speed	1050–1800 rpm	1200–1800 rpm
Rated amplitude of stator phase voltage	563 V	311 V
Rated amplitude of stator phase current	2368 A	16 A
Rated frequency	50 Hz	50 Hz
Stator resistance	1.69 mΩ	0.44 Ω
Rotor resistance	1.52 mΩ	0.64 Ω
Mutual inductance	2.91 mH	79.30 mH
Stator leakage inductance	0.04 mH	3.44 mH
Rotor leakage inductance	0.06 mH	5.16 mH
Time constant of stator flux	1.75 s	0.19 s
Ratio of stator winding and rotor winding	0.369	0.336

TABLE II
SPECIFICATION OF ROTOR-SIDE CONVERTERS

Rated power	400 kW	5.5 kW
Rated amplitude of rotor phase current	915 A	7A
Rated amplitude of rotor phase voltage	305 V	173 V
DC-link capacitor	20 mF	600 μF
DC-link voltage V_{dc}	1050 V	650 V
Switching frequency f_{sw}	2 kHz	5 kHz
Used power module in each arm	1 kA/1.7 kV; two in parallel	50 A/1200 V

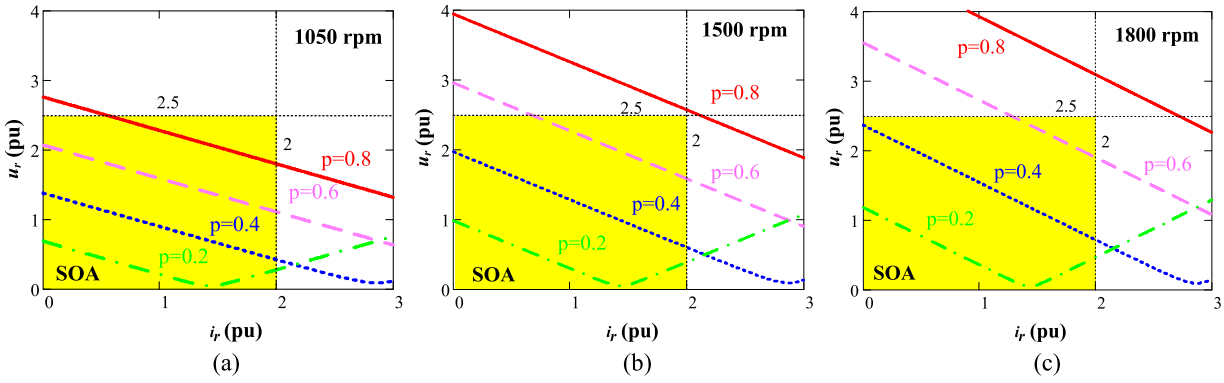

Fig. 6. Factors affecting the rotor voltage during the symmetrical grid fault. (a) 1050 rpm. (b) 1500 rpm. (c) 1800 rpm.

1.7 kV power module, the dc-link voltage should be limited to 1300 V during the transient period. Then, a 2.5 pu rotor voltage is regarded as the limitation of the voltage stress in order to ensure safe operation.

According to (6), the relationship between the rotor current and the rotor voltage can be found by using demagnetizing control, and Fig. 6 illustrates the factors affecting the rotor voltage during a symmetrical fault. In the case of the same rotor speed, it is noted that a more severe dip level leads to a higher rotor EMF, as the natural stator flux is proportional to the dip level. This is shown in Fig. 4(a). Moreover, in the case of the same dip level, it can be seen that a higher rotor speed contributes to a higher rotor EMF because the natural stator flux rotates faster with respect to the rotor side, as expressed in (7). Furthermore, a higher demagnetizing current introduces a lower rotor voltage owing to the fact that the corresponding voltage drop across the rotor impedance counteracts the rotor EMF. In short, it can be found that both a higher dip level and higher rotor speed cause a higher rotor EMF, which hinders the fault ride-through of the DFIG.

On the other hand, the capability of the DFIG RSC can be calculated with various amounts of demagnetizing current, as shown in Fig. 7. Assuming that a maximum 2.0 pu demagnetizing current is applied, the RSC can fully ride-through a symmetrical grid fault at a rotor speed of 1050 rpm. However, if the rotor speed increases to 1500 rpm and 1800 rpm, the DFIG can ride-through a dip level of around 0.8 and 0.7, respectively. Compared to the DFIG capability with 1.0 pu and 2.0 pu demagnetizing current, a higher amount of demagnetizing current facilitates a higher fault ride-through capability. It is evident that the fault ride-through capability of the DFIG is tightly related to the rating of the power converter. However, a higher demagnetizing current increases the thermal stress of the RSC and affects the reliability of the DFIG power converter.

C. Machine Performance During Fault Period

Apart from the safe operation of the DFIG during a faulty condition, the output power and electromagnetic torque are also important indexes, and their analytical equations can be derived by using demagnetizing control. Although the active and reactive power of the DFIG stator is dependent on the stator voltage and current, they can also be expressed in terms of the stator voltage, stator flux, and rotor current according to (3) and (4)

$$P_s + jQ_s = -\frac{3}{2}\frac{1}{L_s}\vec{u}_s^s \cdot \vec{\psi}_s^s + \frac{3}{2}\frac{L_m}{L_s}\vec{u}_s^s \cdot \vec{i}_r^s. \tag{8}$$

During the transient period of the grid fault, the stator flux can be divided into a forced component and a natural component, whereas the rotor current contains only a natural component in the case of demagnetizing control. As a result, the active and reactive power can be derived as

$$P_s = \frac{3}{2}\frac{1}{L_s}\frac{(kL_m+1)(1-p)pU_s^2}{\omega_1}e^{-t/\tau'}\sin(\omega_1 t) \tag{9}$$

$$Q_s = -\frac{3}{2}\frac{1}{L_s}\Big(\frac{(1-p)^2U_s^2}{\omega_1} + \frac{(1+kL_m)(1-p)pU_s^2}{\omega_1}e^{-t/\tau'}\cos(\omega_1 t)\Big) \tag{10}$$

where τ' denotes the modified time constant of the decaying stator flux by using demagnetizing control. It can be seen that the steady-state component of the active power becomes zero, but the steady-state component of the reactive power is absorbed from the power grid, which indicates that the demagnetizing control leads the DFIG to an inductive load. Moreover, the transient components of both the active and reactive power oscillate at the grid frequency, owing to the natural component existing in the stator flux and the rotor current.

As the electromagnetic torque of the induction generator is tightly related to the stator flux and rotor current, it can be derived as

$$T_e = \frac{3}{2}n_p\frac{L_m}{L_s}\mathrm{Im}[\vec{\psi}_s^s \cdot \vec{i}_r^s] = -\frac{3}{2}n_p\frac{L_m}{L_s}\frac{k(1-p)p}{\omega_1^2}U_s^2e^{-t/\tau'}\cos(\omega_1 t) \tag{11}$$

where n_p denotes pole pairs of the induction generator. It is worth noting that the steady-state component of the electromagnetic torque becomes zero, and the transient component also fluctuates at the grid frequency.

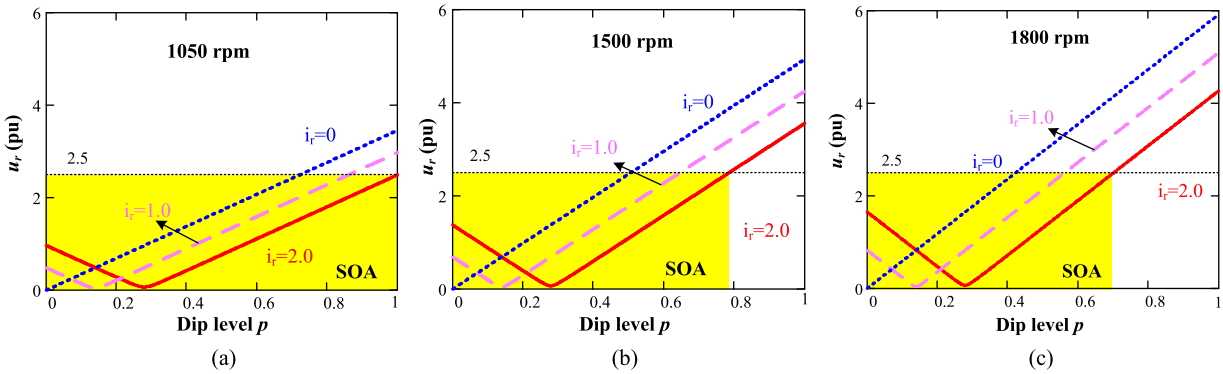

Fig. 7. Capability of the doubly fed induction generator to ride-through various dip levels. (a) 1050 rpm. (b) 1500 rpm. (c) 1800 rpm.

IV. Control Strategy for Reduced Thermal Stress of Power Converter

The control scheme of the RSC during the grid fault occurrence and clearance is shown in Fig. 8, owing to the existence of the natural stator flux. At the instant of the fault occurrence, the control priority of the RSC shifts to inject demagnetizing current, in order to maintain the RSC within its SOA and to accelerate the decay of the natural stator flux. Afterwards, a certain amount of the reactive current is forcibly injected at the stator of the DFIG within dozens or hundreds of milliseconds in accordance with the grid code. This imposes another rotor current stress compared to the residual demagnetizing current. In this section, the effects of the reactive current injection and the residual demagnetizing current are theoretically evaluated and analyzed. By determining the relationship between thermal behavior and the electrical loading of the power semiconductor, a design procedure for the optimized demagnetizing coefficient is proposed. This can achieve a minimum thermal stress of the power devices in the RSC.

A. Effect of Reactive Current Injection

As stated in [10] and [11], different countries may have various response times to the reactive current injection. In this paper, the Spanish grid code is used, and a 150 ms response time is specified [11].

For the DFIG configuration, although the GSC is able to provide the reactive current to meet the grid codes requirement, it induces significantly higher current and voltage stress of the power converter compared to the compensation from the RSC owing to the ratio between the stator and rotor winding of the DFIG [21]. As a result, the GSC contributes to stabilize dc-link voltage during the period of the fault ride-through without the reactive current injection. The required reactive current is fully injected from the stator of the induction generator, which causes an extra current stress seen from the rotor side according to (1) and (3) [25]

$$i_{r\_Q} = -\frac{(1-p)\cdot U_s}{\omega_1 L_m} - \frac{L_s}{L_m}\cdot i_{s\_Q} \tag{12}$$

where i_{s_Q} and i_{r_Q} denote the stator current and rotor current related to the reactive power, respectively.

Fig. 9 shows the effects of the dip level on the stator current and rotor current. This is consistent with the grid codes specified in Fig. 3(b). The stator current increases constantly until the dip level reaches 0.5, and a 1.0 pu reactive current is maintained if the dip level is higher than 0.5. Based on (12), the rotor current changes with the various dip levels. At the normal grid voltage, only a 0.25 pu rotor current can be observed, as it is the magnetizing component of the rotor current, and the active power component is excluded. At a dip level of 0.5, the highest rotor current is reached by a factor of two. The maximum stator current is required by the grid codes, as shown in Fig. 9. Meanwhile, a higher remaining grid voltage also leads to a higher rotor current as expressed in (12). In short, it is evident that at the instant of the reactive current injection, the amplitude of the rotor current is solely determined by the dip level.

B. Effect of Residual Demagnetizing Current

At the instant of a grid fault occurrence, the demagnetizing control is applied, and the demagnetizing current exponentially decreases owing to the decaying natural stator flux. The decaying time constant of stator flux τ' can be deduced as [18]

$$\tau' = \tau_s \cdot \frac{1}{1+\frac{L_m\cdot\omega_1}{p\cdot U_s}\cdot i_r} \tag{13}$$

where the decaying time constant is affected by both the demagnetizing current and the voltage dip level.

The demagnetizing current effect on the natural flux decay is shown in Fig. 10(a) with various dip levels. It is obvious that at the same dip level, a higher demagnetizing current causes a faster decay of the natural stator flux. In addition, a higher dip level induces a longer transient period at the same demagnetizing current. As calculated in Fig. 7, by using a maximum 2.0 pu demagnetizing current, the DFIG system is able to ride-through a symmetrical grid fault at a dip level of 0.7. Under this circumstance, the decaying time constant can be significantly reduced to 140 ms compared with the original stator flux time constant of 1750 ms.

Simultaneously, the residual demagnetizing current i_{r_RES} exponentially decays during the fault period. It is expressed as

$$i_{r\_\mathrm{RES}} = i_{r\_\mathrm{DEM}}\cdot\exp\left(-\frac{t_Q}{\tau'}\right) \tag{14}$$

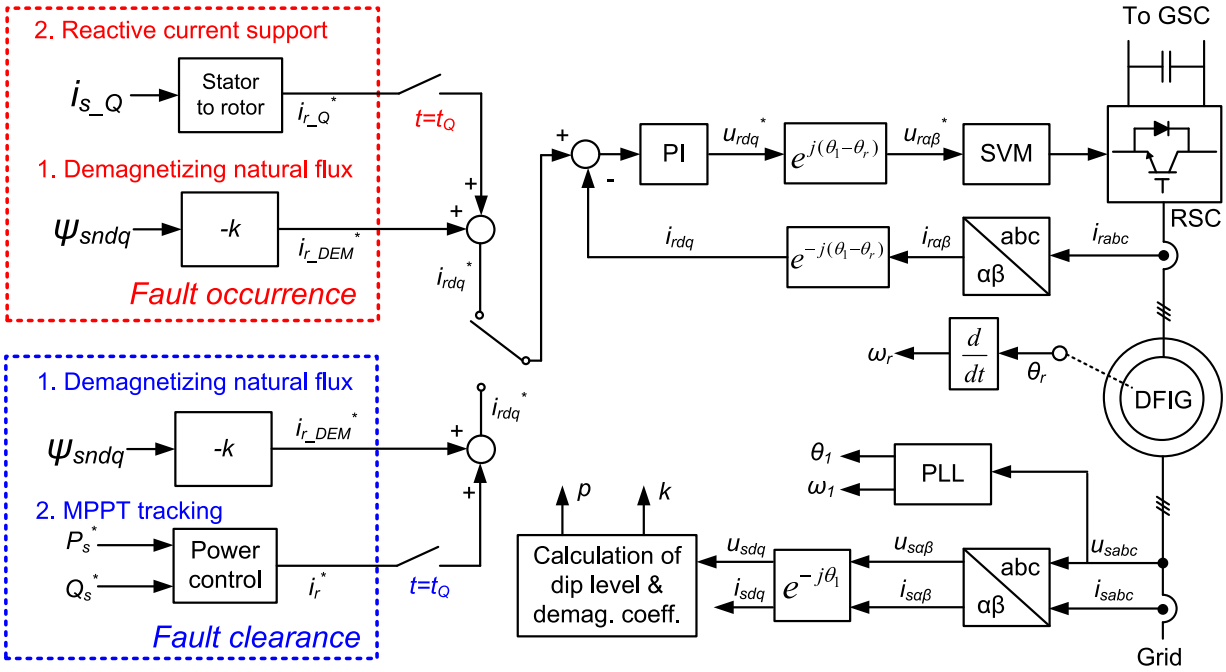

Fig. 8. Control schemes of the rotor-side converter in the cases of the grid fault occurrence and clearance.

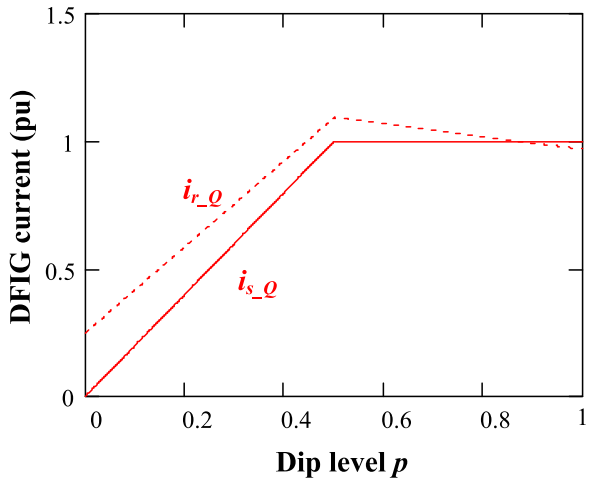

Fig. 9. Requirement of the reactive current injection in terms of the stator current and the rotor current.

where i_{r_DEM} denotes the demagnetizing current at the instant of the fault occurrence, and t_Q denotes the instant of the reactive current injection.

Consequently, the residual demagnetizing current at the instant of the reactive current injection with various initial demagnetizing current is shown in Fig. 10(b) in relation to the voltage dip. It can be seen that although the stator flux can be eliminated earlier with a higher amount of demagnetizing current, a higher residual rotor current may also cause a higher electrical stress of the power semiconductor.

C. Thermal Behavior Estimation of Power Semiconductor

In order to predict the junction temperature of the power semiconductors from the rotor current, a loss model and thermal model of the power semiconductor are required. As illustrated in Fig. 11, loss distribution between the insulated gate bipolar transistor (IGBT) P_T and the freewheeling diode P_D can be obtained with the loss model, and then the junction temperature of the IGBT T_{j_T} and the diode T_{j_D} can be estimated based on the thermal model.

The loss dissipation of the power semiconductor mainly consists of the conduction loss and the switching loss, both of which can be investigated within every fundamental frequency [25]. The conduction loss in each power device P_{con} can be deduced as

$$P_{\mathrm{con}} = f_r \cdot \left(\sum_{n=1}^{N} V_{ce}(|i_r(n)|) \cdot |i_r(n)| \cdot T_1(n) + \sum_{n=1}^{N} V_f(|i_r(n)|) \cdot |i_r(n)| \cdot (T_s - T_1(n)) \right) \quad (15)$$

where the first term denotes the conduction loss of the IGBT P_{T_con}, and the second term denotes the conduction loss of the freewheeling diode P_{D_con}. i_a denotes the sinusoidal current through the power device, T_1 denotes the ON time of the upper leg within a switching period T_s, V_{ce}, V_f denote the voltage drop of the IGBT and the diode during their on-state period. N denotes the carrier ratio - the switching frequency over the fundamental frequency f_r, and the subscript n denotes the nth switching pattern. It is noted that the fundamental frequency changes in the case that the demagnetizing current takes effects.

The space vector modulation is widely used in a three-phase three-wire system due to its higher utilization of the dc-link voltage. In order to guarantee the minimum harmonic, the symmetrical sequence arrangement of the no-zero vector and zero-vector is normally used, and the conduction time of the

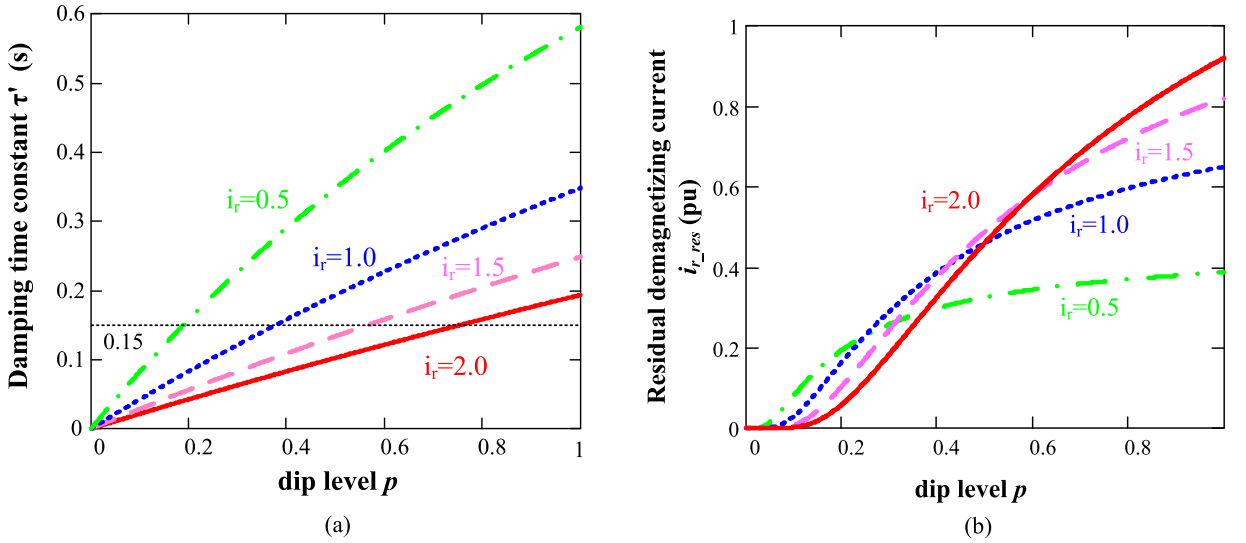

Fig. 10. Effects of the residual demagnetizing current. (a) Relationship between the time constant of the decaying natural flux and the dip level with various demagnetizing current. (b) Residual demagnetizing current at the instant of the reactive current injection.

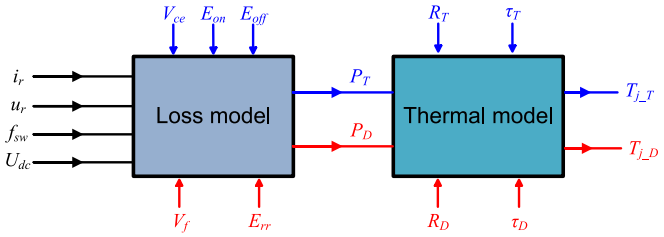

Fig. 11. Approach to estimate the junction temperature of the power semiconductor.

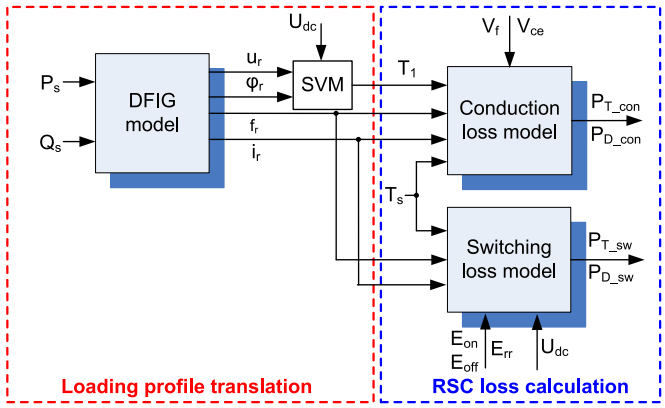

Fig. 12. Block diagram of loss calculation for rotor-side converter equipped with doubly fed induction generator.

upper and the lower switch of leg can thus be deduced based on the converter output voltage vector. Within a fundamental frequency of the converter output current, each IGBT of the same leg only conducts half-period. The direction of the current is relevant to the conduction loss distribution between the IGBT and the diode. As a result, the displacement angle between the output voltage and current is also important.

For the RSC, the phase angle is related to the power factor of the stator-side of the DFIG as well as the DFIG parameters. Neglecting the stator resistance and the rotor resistance, the steady-state DFIG equivalent circuit can be deduced from Fig. 2(a), and the rotor current and voltage can be expressed in terms of the stator voltage and current:

$$\vec{i}_r^{\,s} = \frac{1}{j\omega_1 L_m}\vec{u}_s^{\,s} - \frac{L_s}{L_m}\vec{i}_s^{\,s} \tag{16}$$

$$\vec{u}_r^{\,s} = \frac{sL_r}{L_m}\vec{u}_s^{\,s} - j\frac{s\sigma\omega_1 L_r L_s}{L_m}\vec{i}_s^{\,s} \tag{17}$$

which leads to the displacement angle of the RSC output φ_r.

The switching loss in each power device $P_{\rm sw}$ can be calculated as

$$P_{\rm sw} = \frac{U_{\rm dc}}{U_{\rm dc}^*}\cdot f_r \cdot \left(\sum_{n=1}^{N}\left(E_{\rm on}(|i_a(n)|) + E_{\rm off}(|i_a(n)|)\right) + \sum_{n=1}^{N} E_{\rm rr}(|i_a(n)|)\right). \tag{18}$$

Similarly as (15), the first term denotes the switching loss for the IGBT P_{T_sw}, and the second term denotes the switching loss for the freewheeling diode P_{D_sw}. $E_{\rm on}$ and $E_{\rm off}$ are the turn-on and the turn-off energy dissipated by the IGBT, and $E_{\rm rr}$ is the reverse-recovery energy dissipated by the diode, which are normally tested by the manufacturer at certain dc-link voltage $U_{\rm dc}^*$. It is assumed that the switching energy is proportional to the actual dc-link voltage $U_{\rm dc}$. The block diagram to calculate loss dissipation of the RSC is shown in Fig. 12.

As shown in Fig. 13, the thermal impedance that decides the junction temperature of the power device usually consists of the

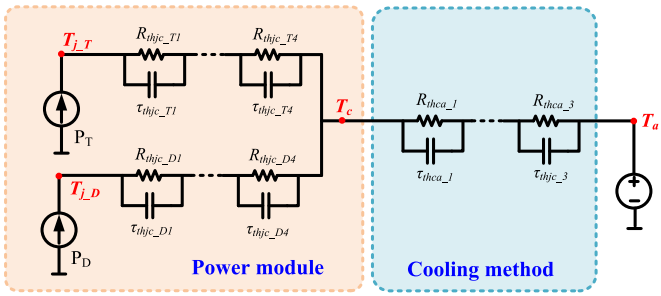

Fig. 13. Thermal model of power semiconductor for power cycles induced by the fundamental frequency.

thermal parameters of the power module itself (from junction to baseplate or case), and thermal integrate material (TIM) as well as the cooling method. Generally, the thermal time constant of a typical liquid cooling system is from dozens of seconds to hundreds of seconds for MW-level power converter, while the maximum thermal time constant of the power device is hundreds of milliseconds. On the other hand, the maximum fundamental period of the rotor current is around several seconds, which implies that the thermal cycling caused by the cooling method can almost be neglected [26]. As a result, for the thermal cycle analysis, the thermal model of the cooling method will only affect the mean junction temperature, but not disturb the junction temperature fluctuation.

As the mean junction temperature $T_{\rm jm}$ and the junction temperature fluctuation dT_j are commonly regarded as the two most important reliability assessment indicators [27]

$$T_{{\rm jm}\_T/D} = P \cdot \sum_{i=1}^{4} R_{{\rm thjc}\_T/D(i)} + P \cdot \sum_{j=1}^{3} R_{{\rm thca}\_(j)} + T_a \tag{19}$$

$$dT_{j\_T/D} = 2P \cdot \sum_{i=1}^{4} R_{{\rm thjc}\_T/D(i)} \cdot \frac{\left(1 - e^{-\frac{t_{\rm on}}{\tau_{{\rm thjc}\_T/D(i)}}}\right)^2}{1 - e^{-\frac{t_p}{\tau_{{\rm thjc}\_T/D(i)}}}}. \tag{20}$$

In (19), $R_{\rm thjc}$ is the thermal resistance from the junction to case of the power module, $R_{\rm thca}$ is the thermal resistance of the cooling method, in which subscripts T and D denote the IGBT and the freewheeling diode, whereas subscripts i and j denote four-layer and three-layer Foster structure for power module and cooling method, respectively. P is the power loss of each power semiconductor, and T_a is the ambient temperature. In (20), $t_{\rm on}$ denotes the on-state time within each fundamental period of current, t_p denotes the fundamental period of the current, and τ denotes the each Foster layer's thermal time constant.

With the key parameters of the power semiconductors listed in Table III, the thermal stress of the IGBT and the diode can be calculated with above mentioned loss and thermal models. During the transient grid fault period, it can be considered that the junction temperature of the power semiconductor is roughly determined by the amplitude of the rotor current.

TABLE III
PARAMETERS USED IN LOSS MODEL AND THERMAL MODEL OF POWER SEMICONDUCTORS

		IGBT	Diode
Loss model	$V_{\rm ce}$ @ 1 kA, T_j = 150 °C (V)	2.45	/
	V_f @ 1 kA, T_j = 150 °C (V)	/	1.95
	$E_{\rm on}$ @ 1 kA, T_j = 150 °C (mJ)	430	/
	$E_{\rm off}$ @ 1 kA, T_j = 150 °C (mJ)	330	/
	E_{rr} @ 1 kA, T_j = 150 °C (mJ)	/	245
Thermal model	Fourth order thermal resistance R (°C/kW)	0.3	0.48
		1.6	3.61
		18	34.6
		3.1	6.47
	Fourth order thermal time constant τ(s)	0.003	0.0002
		0.0013	0.0009
		0.04	0.03
		0.4	0.2

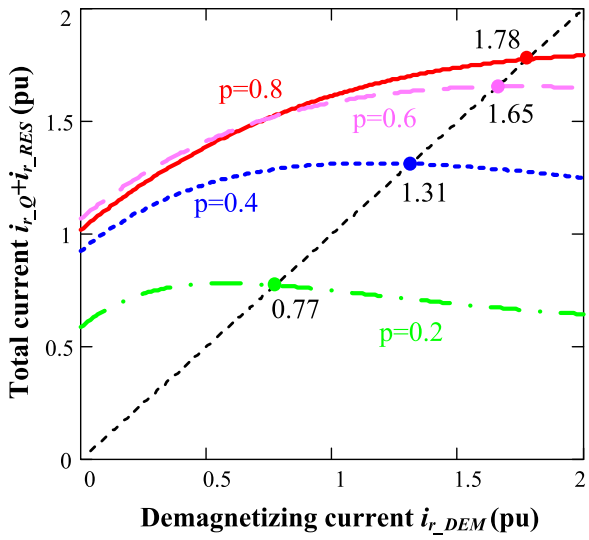

Fig. 14. Relationship between the total rotor current at the instant of the reactive current injection and the initial demagnetizing current.

D. Optimized Demagnetizing Coefficient

As previously mentioned, a suitable amount of demagnetizing current cannot only successfully ride-through the grid fault, but can also provide the reactive current on time. Moreover, the minimum junction temperature during the fault period is also of interest as seen from the reliable operation of the RSC.

The control strategy of the RSC during the grid fault is graphically shown in Fig. 8. Once a fault is detected, the demagnetizing current is provided immediately. At the instant of the reactive current injection, an additional component of the reactive current is expected in addition to the exponentially decaying demagnetizing current. As seen from the similar current loading of the power converter, the optimized demagnetizing coefficient can be obtained when the amplitude of the total rotor current at the instant of the reactive current injection equals the amplitude of the demagnetizing current at the instant of the fault occurrence.

With regard to the reactive component and demagnetizing component of the rotor current, the relationship between the

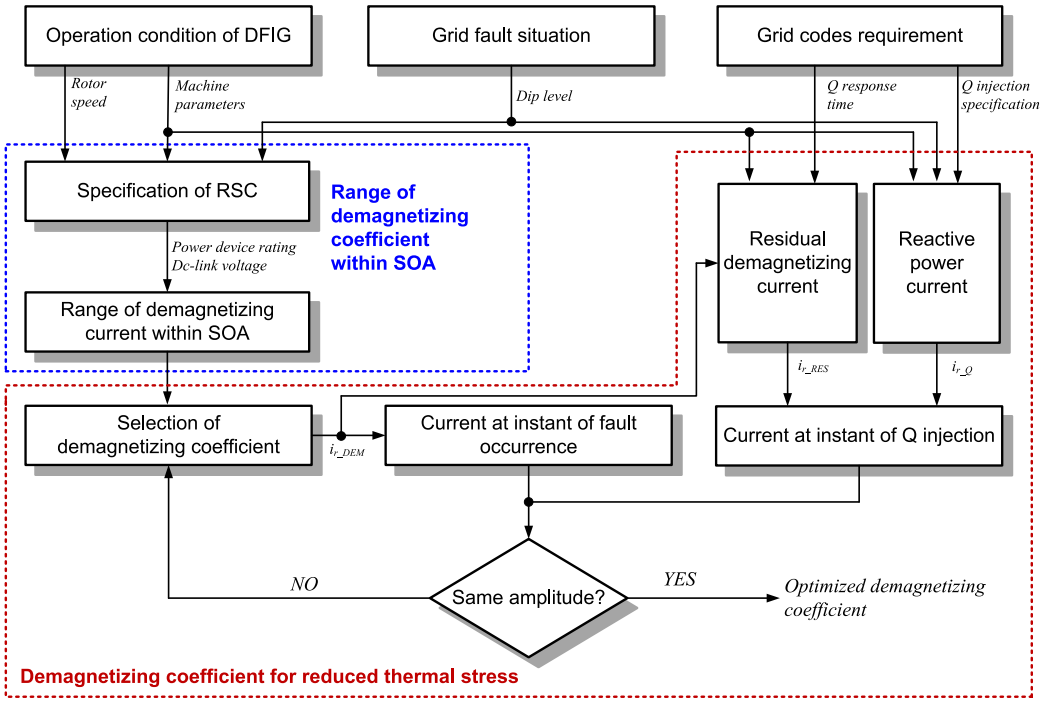

Fig. 15. Flowchart to obtain the optimized demagnetizing coefficient within the safety operation area of the rotor-side converter.

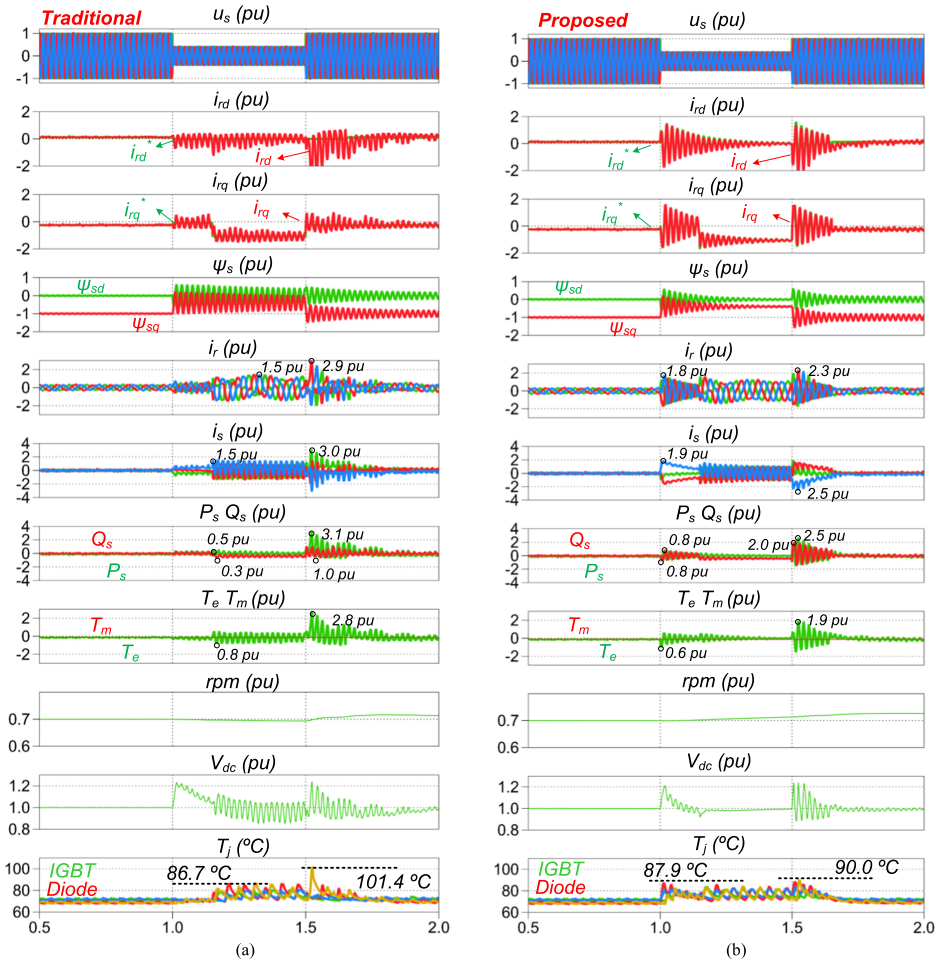

Fig. 16. Simulation results in the case of the DFIG at 1050 rpm to ride-through 0.6 dip balanced grid fault with various control schemes. (a) Traditional vector control. (b) Optimized demagnetizing control.

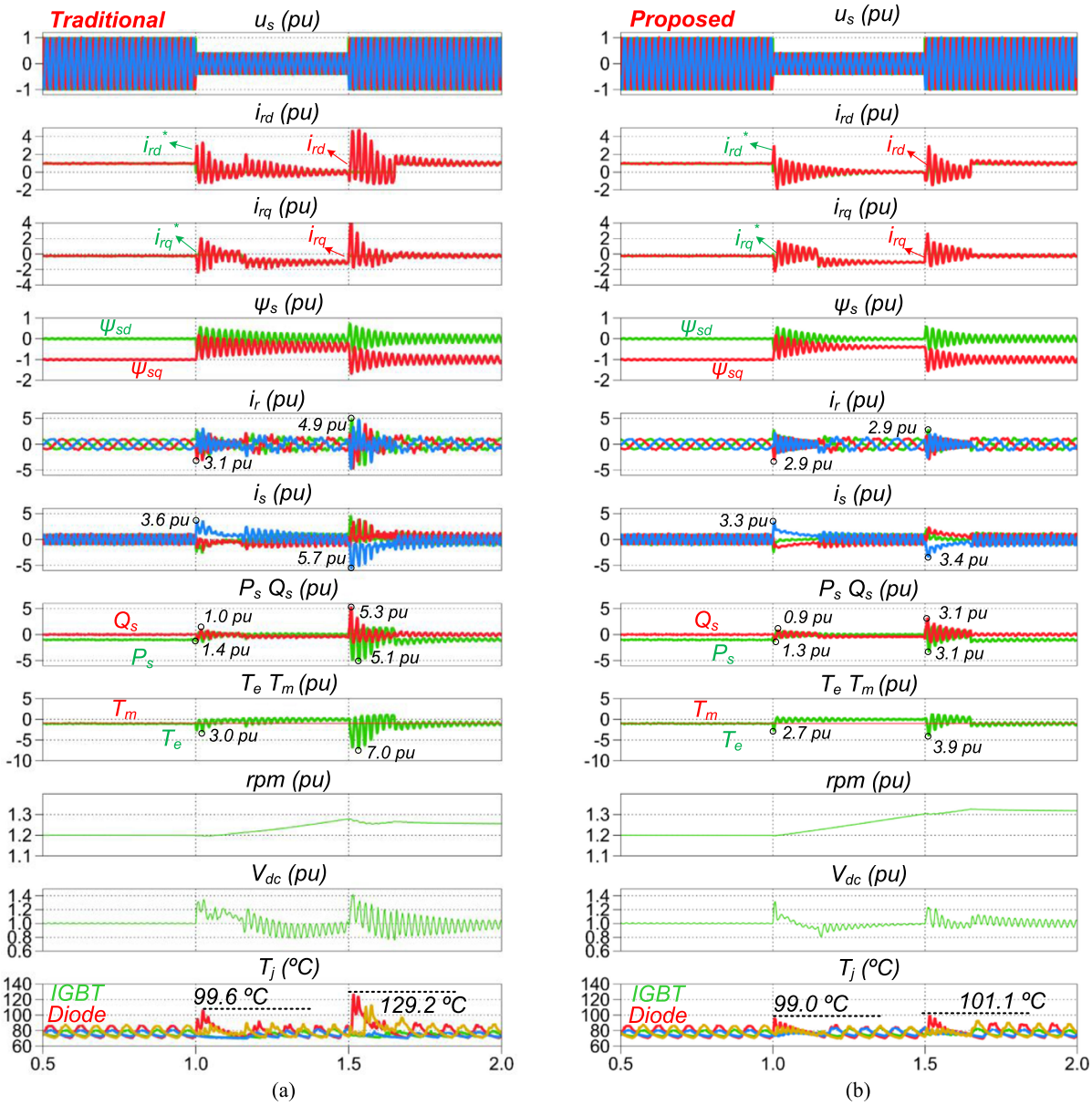

Fig. 17. Simulation results in the case of the DFIG at 1800 rpm to ride-through 0.6 dip balanced grid fault with various control schemes. (a) Traditional vector control. (b) Optimized demagnetizing control.

total rotor current at the instant of the reactive power injection and the initial demagnetizing current at the instant of the fault occurrence is shown in Fig. 14. It can be seen that different demagnetizing coefficients are expected at various dip levels. Specifically, a 1.65 pu demagnetizing current is the optimal choice at a dip level of 0.6, and this amount of the demagnetizing current is sufficient to overcome the over-voltage issue of the dc-link, as shown in Fig. 7.

In order to obtain the reduced thermal stress of the RSC during the symmetrical grid fault, the general procedure to determine the optimized demagnetizing coefficient is summarized in Fig. 15, which is jointly determined by the operation condition of the DFIG, the grid fault situation and the grid codes requirement. Once the dip level of the grid fault is identified by the calculation of the stator voltage under a synchronous reference frame, together with the operation conditions of the DFIG (e.g., rotor speed and machine parameters), the relationship between the rotor current and rotor voltage can be found by using the demagnetizing current control as listed in (6). On the basis of the power device rating of the RSC and the maximum dc-link voltage during the fault ride-through period, the range of the demagnetizing current within the SOA can be mapped at various dip levels. Afterwards, the demagnetizing coefficient can be selected from this range, and the residual component of the demagnetizing current can be calculated with the reactive current response time specified in the grid codes and the parameters of the DFIG. On the other hand, the required reactive current component can be analyzed according to the specification of the

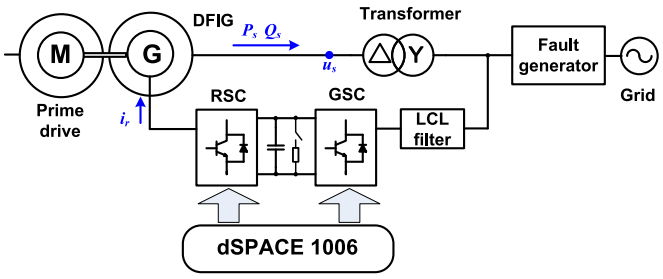

(a)

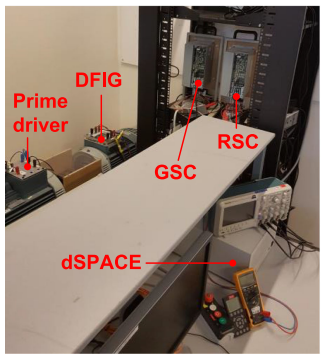

(b)

Fig. 18. 7.5 kW down-scale DFIG test rig. (a) System configuration. (b) Experimental setup.

reactive power injection. In order to achieve the reduced thermal stress of the power device, the optimized demagnetizing coefficient can be designed in the case that the initial demagnetizing current at the fault instant is the same with the sum of the residual demagnetizing current and the reactive current at the instant of reactive power injection.

V. Simulation and Experimental Results

In order to verify the proposed control scheme, a simulation of 2 MW DFIG system is carried out by using the PLECS. The important parameters are listed in Table I. It is noted that the switching frequency of the two power converters is set at 2 kHz. Further, the dc chopper activates if the dc-link voltage is higher than 1300 V, but deactivates if the dc-link voltage is lower than 1100 V. Assuming that a symmetrical grid fault with a dip level of 0.6 occurs for 500 ms, according to the grid codes, a 1.0 pu reactive current is injected after 150 ms of fault detection, and the original active power is provided after 150 ms of fault clearance. For the traditional vector control, once the grid fault is detected, the stator active and reactive power switches to zero before the required reactive current is supplied. During the fault recovery, the stator active and reactive power again switches to zero before the original active power is provided. In the case of the proposed demagnetizing control, the control objective is changed to the elimination of the natural stator flux during the fault period, and the reactive current is additionally supplied after 150 ms of fault detection. Similarly, the demagnetizing current is applied again during the fault recovery, before the original active power is provided at a fault clearance of 150 ms.

At a rotor speed of 1050 rpm, the traditional vector control and the proposed demagnetizing control are compared as shown in Fig. 16. For traditional vector control, as shown in Fig. 16(a), once the grid fault is detected, the rotor current reference is switched to zero in order to minimize the rotor voltage and contribute to the ride-through of the RSC. However, owing to the existence of the natural stator flux, its corresponding rotor voltage exceeds the limit that the dc-link can provide, and the rotor current (i_{rd} and i_{rq}) cannot effectively track its reference (i^*_{rd} and i^*_{rq}). At the instant of the reactive current injection, the maximum junction temperature of the diode appears at 86.7 °C. As shown in Fig. 16(b), when the grid fault occurs, a 1.65 pu demagnetizing current is selected according to Fig. 14. During the fault period, the rotor current is kept almost within the desired value. Moreover, the stator active power, the stator reactive power, and the electromagnetic torque of the DFIG oscillate at the grid frequency and exponentially decay as previously analyzed. The simplified one-mass model of wind turbine is used to describe the relationship between the rotor speed and the electromagnetic torque of the DFIG. With the inertia constant of 3 s caused by the wind turbine and generator [28], assuming the mechanical torque does not change during the grid fault period, the rotor speed increases after the fault occurrence from 0.70 pu to 0.73 pu. Moreover, the mechanical torque is decreased by the wind turbine in the real case, so the variation of the rotor speed may become even smaller [29]. The dc-link voltage is more stable by using the demagnetizing control. Furthermore, compared to the instant of demagnetizing control and the reactive current injection, it is noted that the diode is almost equally stressed, and its maximum junction temperature reaches 87.9 °C. In addition, as the stator flux decays much faster when the proposed demagnetizing control is used, the stator flux, active power, reactive power, and torque almost reach the steady-state at the instant of the fault recovery. This results in a separated evaluation during the grid fault and recovery. However, vector control does not significantly contribute to the acceleration of the natural stator flux decay, which may be superposed at the instant of the fault recovery. Consequently, the maximum junction temperature of demagnetizing control at the instant of the fault clearance is significantly decreased to 90.0 °C, compared to 101.4 °C for vector control.

For the rotor speed at 1800 rpm, the results are shown in Fig. 17. Before the fault occurs, owing to the much higher power through the RSC, it is noted that the power semiconductors are more thermally stressed compared to the 1050 rpm operation. When traditional vector control is applied as shown in Fig. 17(a), since the rotor current is not in control, the maximum rotor current reaches 3.1 pu during the fault period, and the maximum junction temperature of the diode reaches 99.6 °C. When a 1.65 pu demagnetizing current is provided as shown in Fig. 17(b), the rotor current effectively tracks the reference value, and the maximum junction temperature can be slightly reduced to 99.0 °C. In addition, at the instant of the fault recovery, a maximum rotor current of 2.9 pu can be maintained in the proposed control, whereas the rotor current reaches 4.9 pu with the vector control. Thus, the maximum junction temperature of the diode can be significantly reduced to

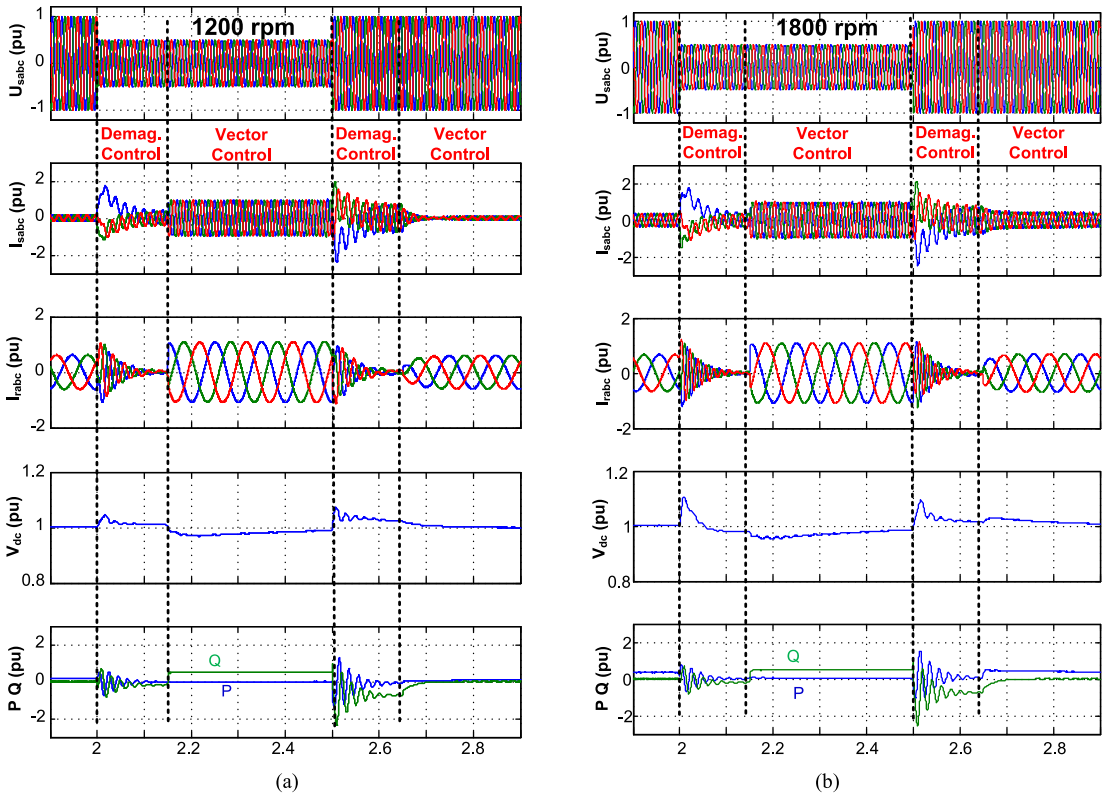

Fig. 19. Simulation results of the down-scale DFIG to ride-through symmetrical grid fault of 0.5 dip level with the optimized demagnetizing coefficient. (a) 1200 rpm. (b) 1800 rpm.

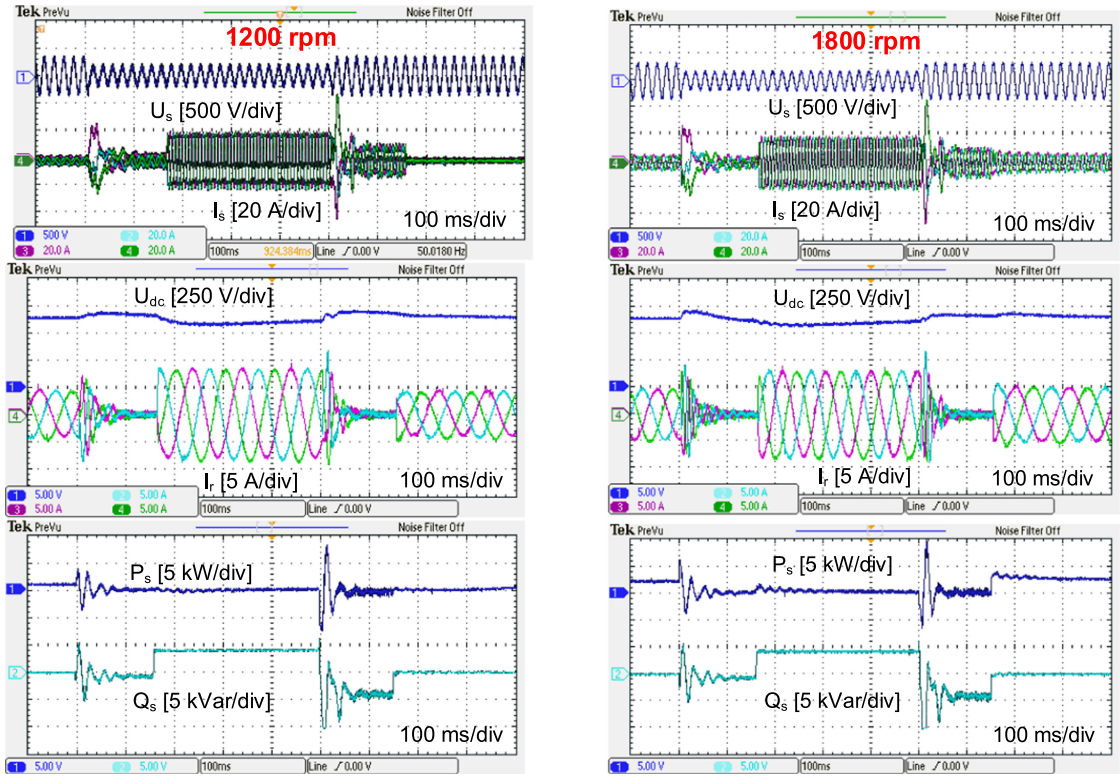

Fig. 20. Experimental results of the down-scale DFIG to ride-through symmetrical grid fault of 0.5 dip level with the proposed demagnetizing control. (a) 1200 rpm. (b) 1800 rpm.

101.1 °C compared to 129.2 °C of the vector control. Thus, the thermal stress of the power semiconductor is considerably improved.

In order to verify the proposed control strategy for the reduced thermal stress of the power converter, some simulations and experiments are performed in a down-scale 7.5 kW DFIG system with the electrical characteristics measurement. As shown in Fig. 18, the DFIG is dragged by a 7.5 kW squirrel-cage motor, back-to-back power converters are established by using two Danfoss 5.5 kW motor drives, and the symmetrical grid fault is generated with the help of the programmable ac power source. The control scheme of both power converters is realized by dSPACE 1006. It is worth noting that the switching frequencies are set at 5 kHz, and the dc-link voltage is regulated at 650 V.

The proposed demagnetizing control is evaluated with a symmetrical fault of 500 ms and dip level of 0.5. According to the demagnetizing coefficient design as shown in Fig. 15, regardless of the rotor speed, the optimized demagnetizing coefficient of 16.3 can be calculated based on the main parameters of the DFIG. With the pu values of the rotor current, dc-link voltage, stator current, and stator voltage defined in Tables I and II, it can be seen that the optimized demagnetizing current becomes 1.13 pu. Meanwhile, a 1.0 pu reactive stator current is provided to fulfill the grid code requirement. As shown in Fig. 19, the corresponding transient performances of the DFIG are simulated in the cases with the rotor speeds of 1200 rpm and 1800 rpm, respectively. For the sub-synchronous operation mode, it can be seen that 0.16 pu active power is generated to the power grid before the fault occurrence. When the fault is detected, the control objective switches to the demagnetizing control for 150 ms, and it can be noted that the initial demagnetizing current becomes 1.13 pu as desired. Once the RSC succeeds to ride-through the grid fault, the vector control is applied with the reactive power injection of 0.5 pu, where the stator current can be observed with 1.0 pu. In the case that the fault is cleared, the demagnetizing current is again used to ride-through the transient situation for 150 ms before the normal vector control is resumed. For the super-synchronous operation mode, 0.33 pu active power is supplied before and after the grid fault. With the same demagnetizing current of 1.13 pu due to the same dip level, the amplitude of the rotor current at the instants of the fault occurrence and reactive current injection keeps the same. Moreover, the dc-link voltage is maintained within 1.15 pu during the entire fault ride-through period.

The same conditions can be tested with the DFIG prototype. When the rotor speed is 1200 rpm as shown in Fig. 20(a), a 1.2 kW active power is provided before the fault occurs. Once the fault is detected, the natural stator flux is controlled for the reduced rotor voltage, and a 7.7 A rotor current (corresponding to 16.1 A stator reactive current) is additionally injected after 150 During the fault recovery, demagnetizing control is again applied to accelerate the natural stator flux decay before the active power prior to the fault is supplied in next 150 ms. As listed in Table I, the time constant of the decaying stator flux is around 190 ms, which can be further decreased to 40 ms with the applied demagnetizing current. As a consequence, it can be seen that the residual demagnetizing current almost becomes minor at the instant of the reactive current injection. Since it is not easy to directly detect the junction temperature of the power device, the rotor current is thereby monitored. This can be regarded as an indirect approach to estimating the thermal stress.

When the rotor speed is 1800 rpm, as shown in Fig. 20(b), a 2.5 kW active power is provided before and after the grid fault, and a 3.75 kVar reactive power is injected during the grid fault. During the period of demagnetizing control, there is no steady-state active power provided, while a certain amount of the reactive power is absorbed by the DFIG according to (9) and (10). It can be observed that, regardless of the rotor speed, the dc-link voltage can be maintained below 750 V during the entire transient period. Moreover, the maximum rotor current reaches 7.9 A between the instant of the grid fault occurrence and the instant of the reactive current injection, which facilitates the reduced thermal stress of the RSC.

VI. Conclusion

This paper addressed existing issues for a DFIG to ride-through a symmetrical grid fault. The internal challenge lies in the direct linking of the DFIG stator and the power grid, and the external challenge arises from the modern grid code requirements. Owing to the much higher EMF caused by the natural stator flux during a symmetrical grid fault, the relationship between the rotor voltage and rotor current in the case of a natural machine is found. With the help of demagnetizing control, the capability of the DFIG can be theoretically calculated at various rotor speeds, with different amounts of demagnetizing current. It is noted that although a higher amount of demagnetizing current leads to a higher fault ride-through capability, it also causes increased thermal stress in the power converter, which may hinder the long-term and reliable operation of the DFIG system.

Considering the grid codes, a design procedure for the optimized demagnetizing coefficient is proposed, in order to keep the maximum rotor current constant between the fault occurrence and the reactive current injection. As the thermal behavior of the power semiconductor is mainly decided by its current, this control strategy is able to achieve a reduced junction temperature during a low-voltage ride-through. It is concluded that, regardless of the rotor speed, the demagnetizing coefficient is related only to the dip level, and simulation and experimental results verify the feasibility of the control scheme for the reduced thermal stress of the power converter during the fault period.

References

[1] Danish Energy Agency. 2016. [Online]. Available: http://www.ens.dk/en
[2] F. Blaabjerg and K. Ma, "Future on power electronics for wind turbine systems," *IEEE J. Emerg. Sel. Topics Power Electron.*, vol. 1, no. 3, pp. 139–152, Sep. 2013.
[3] H. Wang *et al.*, "Transitioning to physics-of-failure as a reliability driver in power electronics," *IEEE J. Emerg. Sel. Topics Power Electron.*, vol. 2, no. 1, pp. 97–114, Mar. 2014.
[4] S. Yang, A. Bryant, P. Mawby, D. Xiang, L. Ran, and P. Tavner, "An industrial-based survey of reliability in power electronic converters," *IEEE Trans. Ind. Appl.*, vol. 47, no. 3, pp. 1441–1451, May 2011.

[5] D. Zhou, F. Blaabjerg, T. Franke, M. Tonnes, and M. Lau, "Comparison of wind power converter reliability with low-speed and medium-speed permanent-magnet synchronous generators," *IEEE Trans. Ind. Electron.*, vol. 62, no. 10, pp. 6575–6584, Oct. 2015.
[6] R. Cardenas, R. Pena, S. Alepuz, and G. Asher, "Overview of control systems for the operation of DFIGs in wind energy applications," *IEEE Trans. Ind. Electron.*, vol. 60, no. 7, pp. 2776–2798, Jul. 2013.
[7] G. Pannell, D. J. Atkinson, and B. Zahawi, "Minimum-threshold crowbar for a fault-ride-through grid-code-compliant DFIG wind turbine," *IEEE Trans. Energy Convers.*, vol. 25, no. 3, pp. 750–759, Sep. 2010.
[8] J. Morren and S. W. H. de Haan, "ride-through of wind turbines with doubly-fed induction generator during a voltage dip," *IEEE Trans. Energy Convers.*, vol. 20, no. 2, pp. 435–441, Jun. 2005.
[9] W. Chen, F. Blaabjerg, N. Zhu, M. Chen, and D. Xu, "Doubly fed induction generator wind turbine systems subject to recurring symmetrical grid faults," *IEEE Trans. Power Electron.*, vol. 31, no. 2, pp. 1143–1160, Feb. 2016.
[10] E.ON-Netz., "Requirements for offshore grid connections," Apr. 2008.
[11] M. Tsili and S. Papathanassiou, "A review of grid code technical requirements for wind farms," *IET Renew. Power Gener.*, vol. 3, no. 3, pp. 308–332, Sep. 2009.
[12] C. Wessels, F. Gebhardt, and F. W. Fuchs, "Fault ride-through of a DFIG wind turbine using a dynamic voltage restorer during symmetrical and asymmetrical grid faults," *IEEE Trans. Power Electron.*, vol. 26, no. 3, pp. 807–815, Mar. 2011.
[13] O. Abdel-Baqi and A. Nasiri, "A dynamic LVRT solution for doubly fed induction generators," *IEEE Trans. Power Electron.*, vol. 25, no. 1, pp. 193–196, Jan. 2010.
[14] J. Yao *et al.*, "Enhanced control of a DFIG-Based wind-power generation system with series grid-side converter under unbalanced grid voltage conditions," *IEEE Trans. Power Electron.*, vol. 28, no. 7, pp. 3167–3181, Jul. 2013.
[15] D. Zhou and F. Blaabjerg, "Minimum junction temperature swing for DFIG to ride-through symmetrical voltage dips," in *Proc. Energy Convers. Cong. Expo.*, 2015, pp. 492–499.
[16] J. Liang, W. Qiao, and R. G. Harley, "Feed-forward transient current control for low-voltage ride-through enhancement of DFIG wind turbines," *IEEE Trans. Energy Convers.*, vol. 25, no. 3, pp. 836–843, Sep. 2010.
[17] F. K. A. Lima, A. Luna, P. Rodriguez, E. H. Watanabe, and F. Blaabjerg, "Rotor voltage dynamics in the doubly fed induction generator during grid faults," *IEEE Trans. Power Electron.*, vol. 25, no. 1, pp. 118–130, Jan. 2010.
[18] D. Xiang, L. Ran, P. J. Tavner, and S. Yang, "Control of a doubly fed induction generator in a wind turbine during grid fault ride-through," *IEEE Trans. Energy Convers.*, vol. 21, no. 3, pp. 652–662, Sep. 2006.
[19] J. Lopez, E. Gubia, E. Olea, J. Ruiz, and L. Marroyo, "ride-through of wind turbines with doubly fed induction generator under symmetrical voltage dips," *IEEE Trans. Ind. Electron.*, vol. 56, no. 10, pp. 4246–4254, Oct. 2009.
[20] L. Wei, R. J. Kerkman, R. A. Lukaszewski, H. Lu, and Z. Yuan, "Analysis of IGBT power cycling capabilities used in doubly fed induction generator wind power system," *IEEE Trans. Ind. Appl.*, vol. 47, no. 4, pp. 1794–1801, Jul. 2011.
[21] D. Zhou, F. Blaabjerg, M. Lau, and M. Tonnes, "Optimized reactive power flow of DFIG power converters for better reliability performance considering grid codes," *IEEE Trans. Ind. Electron.*, vol. 62, no. 3, pp. 1552–1562, Mar. 2015.
[22] K. Ma, M. Liserre, F. Blaabjerg, and T. Kerekes, "Thermal loading and lifetime estimation for power device considering mission profiles in wind power converter," *IEEE Trans. Power Electron.*, vol. 30, no. 2, pp. 590–602, Feb. 2015.
[23] G. Abad, J. Lopez, M. Rodriguez, L. Marroyo, and G. Iwanski, *Doubly Fed Induction Machine-Modeling and Control for Wind Energy Generation*. Piscataway, NJ, USA: IEEE Press, 2011.
[24] C. Lascu, I. Boldea, F. Blaabjerg, and W. Chen, "A class of flux observers for doubly-fed induction generators used in small power wind generation systems," in *Proc. ECCE*, 2013, pp. 2289–2295.
[25] D. Zhou, F. Blaabjerg, T. Franke, M. Tonnes, and M. Lau, "Reduced cost of reactive power in doubly fed induction generator wind turbine system with optimized grid filter," *IEEE Trans. Power Electron.*, vol. 30, no. 10, pp. 5581–5590, Oct. 2015.
[26] M. Marz and P. Nance, "Thermal modeling of power-electronic system," 2000. [Online]. Available: http://www.infineon.com/
[27] D. Zhou, F. Blaabjerg, M. Lau, and M. Tonnes, "Thermal profile analysis of doubly-fed induction generator based wind power converter with air and liquid cooling methods," in *Proc. Eur. Conf. Power Electron. Appl.*, 2013, pp. 1–10.
[28] W. Chen, D. Xu, N. Zhu, M. Chen, and F. Blaabjerg, "Control of doubly-fed induction generator to ride-through recurring grid faults," *IEEE Trans. Power Electron.*, vol. 31, no. 7, pp. 4831–4846, Jul. 2016.
[29] D. Xie, Z. Xu, L. Yang, J. Oestergaard, Y. Xue, and K. P. Wong, "A comprehensive LVRT control strategy for DFIG wind turbines with enhanced reactive power support," *IEEE Trans. Power Syst.*, vol. 28, no. 3, pp. 3302–3310, Aug. 2013.

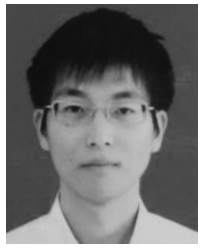

Dao Zhou (S'12–M'15) received the B.S. degree in electrical engineering from Beijing Jiaotong University, Beijing, China, in 2007, the M.S. degree in power electronics from Zhejiang University, Hangzhou, China, in 2010, and the Ph.D. degree in electrical engineering from Aalborg University, Aalborg, Denmark, in 2014.

He is currently a Postdoctoral Researcher with Aalborg University. His research interests include power electronics and reliability in renewable energy application.

Dr. Zhou received the Renewable and Sustainable Energy Conversion Systems of the IEEE Industry Applications Society First Prize Paper Award in 2015, and the Best Session Paper at the Annual Conference of the IEEE Industrial Electronics Society, Austria, in 2013. He serves as a Session Chair for various technical conferences.

Frede Blaabjerg (S'86–M'88–SM'97–F'03) received the Ph.D. degree in electrical engineering from Aalborg University, Aalborg, Denmark, in 1995.

He was at ABB-Scandia, Randers, Denmark, from 1987 to 1988, where he became an Assistant Professor in 1992, an Associate Professor in 1996, and a Full Professor of power electronics and drives in 1998. Since 2017, he has been a Villum Investigator. He has authored more than 500 journal papers in the field of power electronics and its applications. He has co-authored two monographs and edited six books in power electronics and its applications. His current research interest includes power electronics and its applications, such as wind turbines, photovoltaic systems, reliability, harmonics, and adjustable speed drives.

Dr. Blaabjerg was the Editor-in-Chief of the IEEE TRANSACTIONS ON POWER ELECTRONICS from 2006 to 2012. In 2017, he became Honoris Causa with University Politehnica Timisoara, Romania. He was the recipient of 24 IEEE prize paper awards, the IEEE Power Electronics Society (PELS) Distinguished Service Award in 2009, the EPE-PEMC Council Award in 2010, the IEEE William E. Newell Power Electronics Award 2014, and the Villum Kann Rasmussen Research Award 2014. He has been a Distinguished Lecturer for the IEEE PELS from 2005 to 2007, and for the IEEE Industry Applications Society from 2010 to 2011 as well as 2017 to 2018. He was nominated in 2014, 2015, 2016, and 2017 by Thomson Reuters to be one of the 250 most cited researchers in engineering, globally.